Structure and magnetic properties of coprecipitated nickel-zinc ferrite doped rare earth elements of Sc, Dy, and Gd

Li Shiwen (shiwengogogo@st.gxu.edu.cn)
Guangxi University https://orcid.org/0000-0001-8907-8311
Pan Jiatong
Guangxi University
Gao Feng
Guangxi University
Zeng Deqian
Guangxi University
Feng Qin
Guangxi University
He Chunling
Guangxi University
Gjergj Dodbiba
University of Tokyo: Tokyo Daigaku
Yuezou Wei
Guangxi University
Toyohisa Fujita
Guangxi University https://orcid.org/0000-0002-2697-6867

Research Article

Keywords: Structure, Magnetic property, Nickel zinc ferrite, Rare earth, Coprecipitation

Posted Date: March 23rd, 2021

DOI: https://doi.org/10.21203/rs.3.rs-277352/v1

Version of Record: A version of this preprint was published at Journal of Materials Science: Materials in Electronics on April 20th, 2021. See the published version at https://doi.org/10.1007/s10854-021-05928-0.

Abstract

This research is the basic study of temperature-sensitive ferrite characteristics prepared by coprecipitation with doping different typical sizes of rare earth elements. Ni 0.5 Zn 0.5 Re x Fe 2-x O 4 (NZRF) (X = 0.02, 0.05, 0.07 and 0.09) nanoparticles (NPs) doped by Sc, Dy and Gd prepared by chemical coprecipitation method. The structure and properties of Ni 0.5 Zn 0.5 Re x Fe 2-x O 4 were analyzed by various characterization methods. XRD results show that the grain size of Ni 0.5 Zn 0.5 Re x Fe 2-x O 4 is from 10.6 to 12.4 nm, which is close to the average grain size of 13.9 nm observed on TEM images. It is also found that the ferrite particles are spherical and slightly agglomerated in TEM images. FTIR measurements between 400 and 4000 cm -1 have confirmed the intrinsic cation vibration of the spinel structure. The concentrations of nickel, zinc, iron, and rare earth elements have been determined by ICP-AES, and all ions have participated in the reaction. The magnetic properties of Sc, Dy, and Gd 3+ doped NZRF NPs at room temperature are recorded by a physical property measurement system (PPMS-9). It is found that the magnetization can be changed by adding rare-earth ions. When X = 0.07, Gd 3+ doped Ni 0.5 Zn 0.5 Fe 2 O 4 (NZF) exhibits the highest saturation magnetization. The magnetic properties of NZGd 0.07 vary the most with temperature. The thermomagnetic coefficient of NZGd 0.07 nanoparticles stabilized to 0.18 emu/gK at 0-100°C. Hence, NZGd 0.07 with low Curie temperature and the high thermomagnetic coefficient can be used to prepare temperature-sensitive ferrofluid. All the samples exhibit very small coercivity and almost zero remanences, which indicates the superparamagnetism of the synthesized nanoparticles.

1. Introduction

In recent years, due to its unique properties, nano ferrite has been widely used in many technical fields such as microwave devices, biosensors, catalysis, biomedicine and magnetic recording, magnetic drug delivery, and so on [1]. Ferrite is a composite oxide mainly composed of iron oxide and other iron or rare-earth group oxides. The chemical formula of spinel ferrite is generally represented by $MeFe_2O_4$, and Me is usually divalent metal ions, such as Mg^{2+}, Co^{2+}, Ni^{2+}, Mn^{2+}, Cu^{2+}, Cd^{2+}, Fe^{2+}, etc. [2]. The magnetic property of zinc ferrite and nickel-zinc ferrite are typical soft ferrite. NZF is a kind of functional material widely used in modern communication, the Internet, electrical appliances, biomedical, computer circuit, and anti-electromagnetic interference technology [3-6]. N. Boda [7] studied the low-temperature properties of Sm, Er substituted nickel ferrite and cobalt ferrite, and found that the synthesized nickel ferrite showed superparamagnetic behavior, while cobalt ferrite showed soft magnetic behavior. Therefore, this kind of material is expected to be used in the soft magnetic manufacturing industry. P. H. Nam [8] studied the influence of dipole interaction between particles on the heating efficiency of cobalt zinc ferrite under an alternating magnetic field, and found that $Co_{0.5}Zn_{0.5}Fe_2O_4$ nano ferrite has become a potential material for thermotherapy. N. Kaur [9] has synthesized Mn-Zn ferrite NPs with good magnetism and adjustable Curie temperature, and it is considered that Mn-Zn ferrite can be used as the stable temperature-sensitive ferrofluid (magnetic fluid) for heat exchange devices.

The magnetism of ferrite is formed by the direct electron spin exchange between adjacent magnetic atoms. The structural formula of spinel ferrite can be written as $[Zn_x^{2+}Fe_{1-x}^{3+}]_A[Me_{1-x}^{2+}Fe_{1+x}^{3+}]_BO_4$, and the subscripts are tetrahedron (A) and octahedron (B). As shown in Fig. 1, the cell of spinel consists of 8 molecules, including 8 divalent metals, 16 of 3-valent metals, and 32 oxygen. O^{2-} is connected with B site and A site sublattices to form a ferrite face-centered cubic structure[10]. The distance between the two magnetic ions is relatively far, and there are oxygen ions in the middle. Due to the existence of oxygen ions, the ferromagnetic electron spin exchange is formed. This type of exchange is called super exchange in ferromagnetic theory. Because of the super exchange,

the magnetic moments of the magnetic ions on both sides of the oxygen ions are arranged in the opposite direction. The antiferromagnetism of many metal oxides comes from this structure. If the magnetic moments arranged in the opposite direction are not equal and there is a residual magnetic moment, the magnetic property is called ferrimagnetism, or ferrite magnetism.

The magnetic, electrical, catalytic, and optical properties of ferrite depend on the distribution of divalent and trivalent ions at A and B sites [11]. In addition, these properties also vary with the geometry and size of nanoparticles. Most of the Me^{2+} ions occupy the octahedral position, while Zn^{2+} ions tend to stabilize in the tetrahedral position. When $x = 0$, it is inverse spinel structure, in which Fe^{3+} accounts for half in A and B, such as Fe_3O_4 and $NiFe_2O_4$; when $x = 1$, it is orthospinel structure, such as $ZnFe_2O_4$; when $0 < x < 1$, the spinel structure is mixed, such as $MnFe_2O_4$ and $MgFe_2O_4$ [12]. The quality of ferrite can be improved by adding non-magnetic/diamagnetic ions with the same appropriate valence state at points A and point B. Lanthanide (Ce - Y) as a dopant in ferrite is particularly noteworthy [13].

The ionic radius of rare-earth ions (RE^{3+}) (0.086 - 0.106 nm) is much larger than that of Fe^{3+} ions (0.064 nm). In spinel structure, the space of A site is smaller than that of B site (r_A = 0.03 nm, r_B = 0.055 nm); therefore, rare earth ions tend to occupy B site. R.K. Singh [14] studied the properties of Ni-Zn ferrite doped with La, Pr, and Sm by citric acid precursor method. The results showed that the size of ferrite doped with rare earth decreased, the saturation magnetization and coercivity decreased. However, only a small concentration of rare-earth ions can enter the spinel lattice because their ionic radius is larger than that of Fe^{3+}. The high concentration of rare-earth ions can cause structural disorder and form an impurity phase at the grain boundary. S.E. Jacobo [15] synthesized Gd substituted nickel ferrite by combustion method. It was found that only a small part of Gd^{3+} entered the lattice, and the saturation magnetization increased slightly. It is well known that the magnetic behavior of ferromagnetic oxides is largely controlled by the iron-iron interaction (spin coupling of 3d electrons). When RE^{3+} replaces Fe^{3+} ions in spinel ferrite, RE^{3+} interact with Fe^{3+} to form 3d-4f electron spin coupling. The magnetic and electrical properties of ferrite can be improved by the strong interaction between RE^{3+} and Fe^{3+} (3d-4f coupling) [16]. R.A. Pawar [17] studied the properties of Cobalt zinc ferrite doped with Gd. Due to the strong exchange between Gd ($4f^7$) and Fe ($3d^5$), the saturation magnetization and coercivity of cobalt zinc ferrite were improved.

The magnetic behavior of spinel ferrite is strongly affected by many factors, including the change of crystal size, magnetic moment (n_B), preferred site occupation of different ions, and local strain. In addition, disordered cation distribution and super exchange interaction between different ions also affect magnetic properties [18]. The distribution of metal cations at A and B sites depends on the sample preparation method, particle size, type, and the number of cations involved. Common synthetic methods include co-precipitation [19], sol-gel [20], citric acid precursor [21], Microemulsion [22] and solid-state chemical reaction method [23]. Among these methods, coprecipitation is one of the methods for preparing ferrite, which can be used in industry at present [24]. The preparation process is to make a solution of a certain proportion of metal salts in accordance with the ratio and then add appropriate precipitators (such as OH^-, CO_3^{2-}, $C_2O_4^{2-}$, etc.) to precipitate metal ions out [25]. The chemical coprecipitation method can easily control the particle size of prepared NPs, and its operation is simple, and its crystallinity is high [26]. Nanoscale particles can be obtained by controlling the mixing speed, stirring time, working temperature, concentration of precursor, and pH value of the reaction mixture. T.J. Shinde [27] et al. studied the properties of Nd-substituted zinc ferrite and found that the average particle size of ferrite decreased with the

increase of Nd^{3+} content. The room temperature resistivity of zinc ferrite substituted by Nd^{3+} is 10^2 times that of zinc ferrite.

In this paper, in order to meet their application in targeted ferrofluid heat exchanger and drug delivery at near room temperature, magnetic ferromagnetic materials need to have a smaller size, appropriate susceptibility and coercivity, and high-temperature sensitivity, so that the ferrofluid can be used as a hyperthermia medium in an alternating magnetic field to have a better thermal effect. Sc, Gd, and Dy rare earth doped nickel-zinc ferrites were synthesized by and coprecipitation method. The morphology and magnetic properties of rare earth doped NZF were studied with temperature. So that ferrite materials have a wider range of applications.

2. Preparation And Characterization

2.1 Synthesis of ferrite nanoparticles

Nickel chloride ($NiCl_2$), ferric chloride hexahydrate ($FeCl_3 \cdot 6H_2O$), zinc chloride ($ZnCl_2$), sodium hydroxide (NaOH), rare earth chloride, and anhydrous ethanol are purchased from Guoyao Chemical Reagent Co., Ltd. All chemicals are analytical grade, and no further purification is required. Deionized water is used throughout the experiment. $FeCl_3 \cdot 6H_2O$ (3 M), $NiCl_2$ (3 M), $ZnCl_2$ (3 M), $ScCl_3$ (0.3 M) solutions were diluted in 100 ml deionized water according to the appropriate proportion (stoichiometric ratio), and then mixed and stirred for 30 minutes to obtain a homogeneous solution. The mixed solution was placed in a magnetic stirrer, heated to 80 ℃, and continuously stirred. 3 M sodium hydroxide was added to the salt solution mixture drop by drop. The pH was adjusted to 10 - 11. This is due to that non-magnetic and paramagnetic particles will form simultaneously at a pH higher than 13. The reaction was then promoted by stirring for 2 hours and ensuring the complete formation of spinel ferrite [26]. The mixed solution gradually turned brown and precipitated. Thoroughly clean the precipitated ferrite particles with deionized water several times to remove any impurities present in the particles or solvents and reduce the pH to 7. The slurry was obtained by suction filtration and dried in a drying oven for one day and one night. After it was taken out and the powder was ground to use performance study.

2.2 Measurement of structure and magnetic property for ferrite particles

The nanoparticles' crystal structures were investigated by X-ray diffraction (XRD). The composition and structure of the samples were analyzed by Cu-$K\alpha_1$ (λ = 0.154 nm) at room temperature by RIGAKUD/max 2500 V X-ray diffractometer. The voltage of the X-ray tube is 40 kV; the current of the X-ray tube is 150 mA; continuous scanning. Scanning speed: 10 °/min; scanning angle: 20° - 90°. The chemical components of prepared ferrites were analyzed with coupled plasma atomic emission spectrometry (ICP-AES). The intrinsic vibrations of metal complexes were measured by Fourier transform infrared spectroscopy (FT-IR). The Fourier transform infrared spectrometer (IRTRACer-100) performs scanning analysis in 400 - 4000 wavelengths. The surface morphology and particle size of the doped ferrite samples were analyzed by transmission electron microscope (TEM, FEI Tecnai G2 F20). The elemental analysis of particles was measured by energy dispersive spectroscopy (EDS).

Magnetic analysis of the sample was carried out using a physical property measurement system (PPMS-9) vibrating sample Magnetometer (VSM). In addition, the temperature sensitivity of the samples was measured under the magnetic field of 2 T in the range of 225 - 400 K.

3. Results And Discussion

3.1 ICP-AES analysis

The concentrations of Ni^{2+}, Zn^{2+}, $Fe^{3+,}$ and RE^{3+} in the coprecipitated NZRF were determined by ICP-AES, and the results are listed in Table 1. Almost all initial metal elements in the solution to react were included in the coprecipitated NZRF particles. The measured metal ion concentration is in almost agreement with the x in $Ni_{0.5}Zn_{0.5}Re_xFe_{2-x}O_4$. Most of the rare earth ions could be dopFed in precipitated ferrite by considering the initial metal concentration for the reaction.

Table 1 Results of the ICP-AES analysis conducted on $Ni_{0.5}Zn_{0.5}Re_xFe_{2-x}O_4$ (RE = Sc, Gd, Dy, x = 0.02, 0.05, 0.07 and 0.09).

Mole ratio(M)	NZSc				NZGd				NZDy			
Initial RE	0.02	0.05	0.07	0.09	0.02	0.05	0.07	0.09	0.02	0.05	0.07	0.09
Ni	0.59	0.56	0.59	0.56	0.56	0.57	0.57	0.56	0.53	0.55	0.58	0.51
Zn	0.59	0.55	0.56	0.55	0.56	0.57	0.56	0.56	0.54	0.56	0.58	0.51
Fe	2.25	2.02	2.23	2.10	2.28	2.22	2.18	2.16	2.16	2.08	2.10	1.97
Re	0.02	0.06	0.08	0.10	0.02	0.06	0.08	0.11	0.01	0.05	0.08	0.10

3.2 XRD analysis

The X-ray powder diffraction pattern of NZF doped by Sc, Gd, and Dy are shown in Fig. 2(a), (b), and (c), respectively. The XRD patterns are cubic spinel ferrite without any impurity peak. All diffraction peaks can be represented by the Fd-3m space group [28]. The positions of the characteristic peaks (220), (311), (400), (422), (511), (440) are consistent, and the diffraction intensity is the strongest on the (311) plane, which confirms that the substituted rare-earth ions are completely dissolved into the host lattice. The X-ray density is calculated by the following formula (Eq. 1:

$$\rho_X = \frac{8M_W}{N_A a^3} \qquad (1)$$

where M_W is the molecular weight, N_A is the Avogadro constant, and 8 is the number of atoms in the unit cell of the spinel lattice.

The average grain size was calculated by the Debye Scherrer equation (Eq. 2):

$$D = \frac{k\lambda}{B\cos\theta} \qquad (2)$$

 = 0.89 (Scheler constant). X-ray wavelength = 0.154 nm. B is the half-height width of the diffraction peak. The formula is Bragg diffraction angle, and the unit is the angle. The average grain size of the different doped amounts is shown in Fig. 2(d). The large peaks of radius are shown in the rare earth doped amount of X=0.05 for $Ni_{0.5}Zn_{0.5}Re_xFe_{2-x}O_4$ (NZRF), and the radius increases more at x = 0.09 for doped Gd and Dy.

The particle size, the lattice constant, and the density calculated by XRD are listed in Table 2. The X-ray density of the synthesized NZRF is 5.21 to 5.44 g/cm^3. The density of Sc doped NZRF is almost the same at x, while the density of Gd and Dy doped gradually increases as x becomes larger. Due to grain boundary aggregation, RE^{3+} ions compress the spinel lattice and increase the lattice density, as shown in Gd and Dy. In addition, with the doping of rare-earth ions, the vacancy amount of nearby metal ions increases, which will lead to an increase in

density. The lattice constant of rare-earth-doped ferrite increases. The substitution of RE^{3+} in spinel structure can also lead to vacancy, distort the symmetry of tetrahedron and octahedron, and then affect the lattice parameters and bonding length. Therefore, it is reasonable to increase the lattice parameters of ferrite with rare-earth. The grain size of NZRF NPs ranged from 10.6 nm to 12.4 nm.

The results show that the particle size of Ni-Zn ferrite is 9.7 nm without any rare earth elements, and increases with the doping of rare earth elements. When Sc^{3+} (0.73 Å), Gd^{3+} (0.98 Å), and Dy^{3+} (0.91 Å) with larger ionic radius enter the spinel structure, they will occupy the octahedral space (B site) composed of six O^{2-}, and replace Fe^{3+} (0.65 Å), which will inevitably lead to lattice distortion, increase the lattice constant and the average grain size [29]. Due to the different solubility of these three rare earth elements, their maximum particle size concentration is also different. For the above-mentioned Fig. 2(d), in the Sc and Gd doped samples, the grain size increases and then decreases with the increase of ion concentration, reaching the maximum value at 0.09. However, the particle size of Dy doped NZRF is the largest at 0.05. After further increasing the rare earth concentration, the rare-earth ions will no longer dissolve in the spinel lattice and begin to diffuse to the grain boundary. They form an ultra-thin layer around the grain boundary, cause stress on the grain boundary, and reduce the grain size and lattice parameters [30]. When Sc^{3+} and Gd^{3+} ions are doped into Ni-Zn ferrite, more energy is needed in the mass transfer process, which hinders the growth of ferrite grains. However, when the amount of Sc^{3+} and Gd^{3+} ions increases, some trivalent ions accumulate in the grain boundary region, and the amount vacancy of metal ions increases nearby to maintain the charge balance, which will lead to the acceleration of grain boundary movement. Therefore, the ferrite grain size increases with the addition of rare earth ions [31]. In addition, as the energy required for rare earth elements to enter the spinel lattice is different, the reason for the decrease of grain size in rare-earth-doped samples is that the energy needed for RE^{3+} to enter in the lattice and form RE^{3+}-O^2 bonds is greater than the energy that Fe^{3+} enters the lattice and forms Fe^{3+}-O^2 bonds. The energy required for crystallization is consumed in the combination of rare earth and oxygen ions [32]. Therefore, the ferrite doped with rare earth elements needs a higher temperature to maintain the nucleation and grain growth. Compared with pure Ni-Zn ferrite, RE^{3+} substituted Ni-Zn ferrite has higher thermal stability; therefore, it needs more energy to complete the crystallization and grain growth of the sample doped with RE^{3+} [33].

Table 2 Structural parameters of $Ni_{0.5}Zn_{0.5}Re_xFe_{2-x}O_4$ NPs.

Content	NZF	NZSc				NZGd				NZDy			
	0	0.02	0.05	0.07	0.09	0.02	0.05	0.07	0.09	0.02	0.05	0.07	0.09
D_{XRD} (nm)	9.7	10.6	11.9	11.5	12.1	10.3	11.3	10.9	12.0	11.7	12.4	12.0	11.5
a (Å)	8.44	8.46	8.46	8.45	8.45	8.44	8.45	8.45	8.45	8.43	8.46	8.35	8.45
ρ_X (g/cm^3)	5.26	5.24	5.21	5.22	5.21	5.29	5.35	5.40	5.43	5.32	5.34	5.59	5.44

3.3 FTIR analysis

The infrared spectrum of spinel ferrite consists of two characteristic stretching vibrations corresponding to the intrinsic vibration of metal complexes. M. Sertkol [34] has reported that there are two main wide metal-oxygen bands in the infrared spectra of all spinel ferrites. The highest one usually observed in the range of 600-500 cm^{-1} corresponds to the intrinsic stretching vibration of the metal at the tetrahedral position, while the low band, usually observed in the range of 450 - 385 cm^{-1}, is designated as octahedral metal stretching vibration. It can be used to infer the structural study and redistribution of cations between the octahedral and tetrahedral sites of spinel structure in Ni-Zn ferrite particles. The samples were analyzed by FTIR in the range of 400 - 4000 cm^{-1}. The infrared absorption spectra of NZRF doped by Sc, Gd, and Dy are shown in Fig. 3(a), (b), and (c), respectively. The characteristic peak intensity vibration at 419cm^{-1} is the intrinsic stretching vibration of Sc–O, Ni–O, and Fe–O at B

site (octahedron) in ferrite, while the characteristic peak at 570 cm^{-1} corresponds to the position of Fe–O and Zn–O at A site (tetrahedron), therefore spinel structure can be considered in the prepared samples [35]. The peak spectrum at 1620 cm^{-1} is –OH, which is caused by the adsorption of –OH on the surface of nanoparticles by the coprecipitation method. The broadband absorption peak at about 3400 cm^{-1} can be attributed to the presence of the –OH group in the sample due to the symmetrical and antisymmetric stretching of water. In addition, the peak value at 2378 cm^{-1} is H–O–H bending vibration caused by free or absorbed water. Bands related to the structure of metal chloride were observed at 1479 and 1365 cm^{-1}. In the case of rare-earth-doped ferrite, the intensity of these two absorption peaks is related to their ability to form surface chloride structure [36].

3.4 TEM analysis

The grain nucleation and crystal growth of ferrite are changed by doping RE^{3+}. When the doping amount reaches a certain amount, the ferrite grain morphology will be destroyed. The surface morphology and particle size of Gd^{3+} doped Ni-Zn ferrite samples were analyzed by TEM (FEI TECNAI G2 F20). The photograph of particles is shown in Fig. 4(a), HRTEM images of representative $NZGd_{0.07}$ nanoparticles, and SAED pattern of the corresponding $NZGd_{0.07}$ are shown in Fig. 4(b) and (c), respectively. In Fig. 4(b), the measured width of the lattice fringes is 0.255 nm, which corresponds to the spacing of the (311) plane shown in XRD. The observed microcrystalline lattice fringes confirm the high crystallinity of nanoparticles in ferrite samples.

In Fig. 4(c), six of them correspond to (200), (311), (400), (422), (511), and (440) planes in ferrite crystals. The arrangement order of the diffraction ring is consistent with that observed in XRD data, so the phase purity of the ferrite sample is determined by plane calibration. Similarly, the ring designated in the SAED mode indicates the polycrystalline nature of the sample.

The particle size distribution calculated by the software is shown in Fig. 4(d). It can be observed from Fig. 4(a) that the particles are cubic and spherical, with sizes ranging from 8 nm to 25 nm, with slight to moderate agglomeration. The distribution size of nanoparticles was expressed by the histogram, and the average particle size was 13.93 nm, which was slightly larger than the previous XRD calculation results. Meanwhile, it also verified that the samples had an agglomeration, so the observed particle size was larger than the average grain size calculated by Scherer's formula. EDS of $NZGd_{0.07}$ detected Ni, Zn, Fe, and Gd at the same particle area as shown in Fig. 4(e), no other impurities were found.

3.5 Magnetic analysis

Magnetization (*Mr*), remanent magnetization (*Mr*), and coercive force (*Hc*) obtained by the hysteresis loops (M-H) of Sc, Gd, Dy doped Ni-Zn ferrites at room temperature (293 K) are shown in Fig. 6(a), (b) and (c), respectively. In the magnetic field range of ± 0.5 T, a PPMS-9 VSM was used to measure the magnetization at room temperature. Synthesized ferrites particles exhibit values of M_S varying in the ranges of 12.2-36.1 emu/g, 12.4 - 41.4 emu/g and 21.2 - 33.6 emu/g for $Ni_{0.5}Zn_{0.5}Sc_xFe_{2-x}O_4$, $Ni_{0.5}Zn_{0.5}Gd_xFe_{2-x}O_4$ and $Ni_{0.5}Zn_{0.5}Dy_xFe_{2-x}O_4$, respectively. The values of remanent magnetization (*Mr*) are in the intervals of 0.03 - 0.72 emu/g, 0.01 - 0.78 emu/g, and 0.05 - 0.47 emu/g for Sc, Gd, and Dy substituted NZF, respectively.

M_S was obtained by M and $1/H^2$ curve. The saturation magnetization (M_S), residual magnetization (*Mr*), coercivity (H_C), Mr/M_S, and magnetic moment of all samples are listed in Table 3. It can be found that the saturation magnetization is improved and large after doping rare earth elements. This result is consistent with that of Ce-

substituted Ni-Zn ferrite prepared by G. Umapathy by combustion method [37]. It can be seen from Fig. 6(a) that the saturation magnetization of Sc, Gd, and Dy doped Ni-Zn ferrites reach the maximum at the contents of 0.05, 0.07, and 0.07, and the saturation magnetization is 38.2, 41.4, and 33.6 emu/g, respectively. A very small coercivity field and almost zero remanences were observed in all samples, which represented the superparamagnetism of the NPs [38].

Generally speaking, trivalent ions strongly tend to occupy the B site, while divalent ions prefer A and B sites. The degree of substitution of A and B by different ions depends on the matrix and ion radius. Zn^{2+} and Fe^{3+} ions have A-A exchange at tetrahedral sites, while Ni^{2+}, Fe^{3+}, and RE^{3+} ions have B-B interactions at octahedral sites. Both the tetrahedral and octahedral ions have A-B super exchange interaction. The A-B super exchange interaction between ions at tetrahedral and octahedral sites is superior to A-A and B-B interactions [39]. When Sc^{3+} (0.73 Å) and Gd^{3+} (0.94 Å) with a larger ionic radius replaced Fe^{3+} (0.65 Å) at Point B, the distance between ions was reduced, which would lead to enhanced A-B exchange and increased magnetism. In addition, the change of magnetic moment ( ) can explain the behavior of M_S. It is well known that the exchange interaction between A and B sites in ferrite directly affects the change of value. The experimental values of magnetic moment ( ) per unit of the formula are derived as follows (Eq. 3):

$$n_B = \frac{M_W M_S}{N_A \mu_B} \qquad (3)$$

where M_W is the molecular weight and M_S is the saturation magnetization in emu/g. N_A is Avogadro constant. is a Bohr magneton with a value of 9.27×10^{-24} J·T^{-1}.

As shown in Table 3, the magnetic moment of the doped sample is higher than that of the undoped sample, which can be used to explain the higher M_S value of the substituted sample and the enhanced super exchange interaction of the doped samples [40]. It can be seen from Fig. 6 that with the increase of rare-earth ion content, the magnetization decreases when the magnetization increases to a critical value. The main reason is that Gd^{3+}(7 μ_B) replaces Fe^{3+}(5 μ_B) in an octahedral position (B site), and Gd^{3+} has higher spin magnetic moment ions than Fe^{3+}. The substitution of Gd^{3+} ions at the B site will affect the interaction between Ni–O–Gd ions, and affect the sublattice exchange energy between Ni–O–Fe [41]. The phenomena are the same for the other two rare-earth ions. However, With the increase of the concentration of RE^{3+}, the saturation magnetization decreases. The saturation magnetization of the three kinds of rare earth doped ferrite begins to decrease at different critical values due to the limited solubility of RE^{3+}. The results show that when the concentration of rare-earth ions is high, the RE^{3+} with a larger radius cannot completely replace the B site. Some ions may gather at the grain boundary to form a second phase and hinder the movement of the domain wall. In the process of domain wall motion, the influence of the second phase on the domain wall motion should be greater than that of the external magnetic field. As the domain wall motion becomes more difficult, the saturation strength decreases [31]. In addition, the magnetic moment of rare-earth ions comes from 4f electrons, which is effective only when the temperature is lower than 40 K [42]. Therefore, their magnetic dipole orientations are disordered at room temperature and exhibit paramagnetic behavior [43]. This means that the rare-earth ions in ferrite lattice replace the magnetic ions at the B site, which leads to a decrease in magnetism.

The coercivity of ferrite is a microstructure property, which is affected by strain, defect, porosity, and magneto-crystalline anisotropy [43]. The anisotropy constant K_1 depends on the rare earth ion content x. According to the Stoner Wohlfarth model, the coercivity and anisotropy constant K_1 are connected by the following relationship (Eq. 4) [44].

$$K_1 = \frac{1}{2}\mu_0 H_C M_S \qquad (4)$$

μ_0 is the vacuum permeability. According to Stoner Wohlfarth's theory, coercivity increases with the decrease of magnetization. In accordance with the conclusion obtained in this paper, the relationship between H_C and M_S is inversely proportional. It can be seen from the figure that the coercivity of ferrite doped with rare earth elements increases because RE^{3+} have a large single-ion anisotropy. When rare earth ions partially replace Fe^{3+} ions, the magnetic anisotropy and the coercivity become greater. With the increase of rare-earth doping content, the coercivity first decreases and then increases. On the one hand, with the increase of grain size, larger grain size often contains more domain walls. When the magnetic moment and magnetic anisotropy of a single particle decrease, a stronger magnetic field is needed for magnetization reversal. This behavior continues until the critical size becomes a single domain, beyond which the single domain particle will split into multiple domains [41]. In a weak external magnetic field, the domain wall motion and magnetization rotation will lead to the magnetization process of multi-domain samples. This will reduce coercivity.

The ratio *Mr*/*Ms* is called squareness ratio (SQR), which determines the magnetic hardness of materials and the existence of group exchange between grains [45]. It is reported that when $0.05 < Mr / Ms < 0.5$, the sample has a single domain magnetostatic coupling [46]. The squareness ratio of NZRF spinel ferrite is calculated, and the results have been shown in Table 3. The squareness ratio ranges from 0.001 to 0.019, indicating the multi-domain structure of the particles in which domain wall movement allows for an easier change in orientation with the applied field.

The variation of magnetization with temperature in the range of 225 - 400 K was recorded at an applied magnetic field of 2 T. The magnetization versus temperature of NZF doped by Sc, Gd, and Dy are shown in Fig. 7(a), (b), and (c), respectively. In the rare earth doped ferrites, most magnetization change versus temperature shows in $NZSc_{0.05}$, $NZGd_{0.07,}$ and $NZDy_{0.07}$ for each rare earth doping. According to the dependence of saturation magnetization on temperature, Curie temperature of Ni-Zn ferrite has been roughly estimated at Tc = 425 K. It can be seen from Fig. 7 that with the increase of temperature, the decrease of magnetization is due to the disorder of the magnetic spin phase caused by the increase of heat energy [47]. Thermomagnetic coefficient K_T ($K_T = dM/dT$) is calculated from the first derivative of the temperature-dependent magnetization curves of each component. As can be seen from Fig. 7(d), when the temperature is close to the Curie temperature, the thermomagnetic coefficient K_T decreases rapidly with the temperature increase. The magnetic properties of $NZGd_{0.07}$ vary the most with temperature, and the thermomagnetic coefficient K_T increases from 0.13 emu/gK to 0.24 emu/gK. The magnetic properties of $NZGd_{0.07}$ are more varied than Dy doped cobalt-zinc ferrite obtained by S. Urcia-Romer [48]. The stability of ferrofluid at operating temperature and the vapor pressure of carrying liquid determine the practical application of ferrofluid. As can be seen from Fig. 7(d), the thermomagnetic coefficient of $NZGd_{0.07}$ nanoparticles stabilized to 0.18 emu/gK at 0 - 100 ℃. As a result, ferrofluid can operate at temperatures around 0 - 100 ℃ without losing

much stability and can be used for energy conversion applications. In addition, when ferrofluid is used to treat cancer, it quickly reaches the specified temperature and remains stable without harming human tissues.

Table 3 Saturation magnetization (M_S), remanence (Mr), coercivity (Hc) of nickel-zinc ferrite doped with different concentrations of different rare earth elements at room temperature.

Content	NZF	NZSc				NZGd				NZDy			
	0	0.02	0.05	0.07	0.09	0.02	0.05	0.07	0.09	0.02	0.05	0.07	0.09
Ms(emu/g)	27.4	31.1	38.2	34.6	12.2	29.9	38.6	41.4	15.0	21.2	31.7	33.6	26.3
Mr(emu/g)	0.33	0.36	0.72	0.70	0.03	0.35	0.74	0.78	0.01	0.05	0.42	0.47	0.29
Hc(Oe)	14.73	17.02	15.47	15.26	16.00	16.34	15.22	15.14	15.39	16.23	15.52	15.32	15.40
Mr/Ms	0.012	0.011	0.019	0.020	0.002	0.012	0.019	0.019	0.001	0.002	0.013	0.014	0.011
$n_B(\mu_B)$	1.17	1.33	1.62	1.47	0.52	1.28	1.68	1.82	0.53	0.91	1.38	1.48	1.17

4. Conclusion

Dy, Gd, and Sc doped Ni-Zn ferrites were successfully prepared by the coprecipitation method. The effects of doping Dy^{3+}, Gd^{3+}, Sc^{3+} ions on the structure and properties of Ni-Zn ferrite were analyzed in detail. Rare-earth element doping plays an important role in changing the structure and magnetic properties of Ni-Zn ferrite. XRD analysis confirmed that the samples were cubic spinel structure, single-phase. Rare earth doping increases the grain size of ferrite. The grain size of ferrite without doping is 9.7 nm, while that of rare-earth-doped ferrite is from 10.6 to 12.4 nm. The grain size of doped ferrite increases and shows the first peak at 0.05 RE content. At the same time, it was observed by TEM that the Ni-Zn ferrite particles' average grain size was 13.93 nm, which was similar to the XRD results. The intrinsic stretching vibration of B site (octahedral) RE–O, Ni–O, and Fe–O and the intrinsic stretching vibration of Fe–O and Zn–O at A site tetrahedron) were observed at 419 cm^{-1} and 570 cm^{-1}, respectively, which confirmed the formation of metal oxides. The magnetization results showed that the M_S of Ni-Zn ferrite was increased by doping rare earth elements, and the maximum saturation magnetization of $NZGd_{0.07}$ was 41.4 emu/g. When the saturation magnetization of ferrite increases, the coercivity decreases. The coercivity of all ferrites is about 16 Oe, and the remanent magnetization is almost zero, which indicates the superparamagnetic of the synthesized ferrite. The increase of M_S and Mr is also attributed to the increase of grain size, the enhancement of super exchange interaction, and the increase of . With the rise in temperature, the magnetization of Ni-Zn ferrite decreases. The magnetic properties of $NZGd_{0.07}$ vary the most with temperature, and the thermomagnetic coefficient K_T increases from 0.13 emu/gK to 0.24 emu/gK. $NZGd_{0.07}$ with low Curie temperature and the high thermomagnetic coefficient can be used to prepare temperature-sensitive ferrofluid. It can be used in heat exchanger, magnetic hyperthermia, switch and so on at near room temperature.

Declarations

The authors report no declarations of interest.

Author Contributions

Shiwen Li: Conceptualization, Methodology, Analysis, Data curation, Writing, Jiaotong Pan: data curation, Feng Gao, Deqian Zeng, Feng Qin and Chunlin He: Discussion of the experiment, Gjergj Dodbiba: Correction of writing, Yezou Wei: Conceptualization, Toyohisa Fujita: Supervision

Acknowledgments

One part of this work was supported by the Natural Science Foundation of China [NSFC 21976039].

References

[1] P. Thakur, R. Sharma, V. Sharma, P.B. Barman, M. Kumar, D. Barman, S.C. Katyal, P. Sharma, Gd doped Mn-Zn soft ferrite nanoparticles: Superparamagnetism and its correlation with other physical properties, Journal of Magnetism and Magnetic Materials, 432 (2017) 208-217.

[2] A.C.F.M.C. A, E.T. B, M.R.M. B, R.H.G.A.K. B, Synthesis, microstructure and magnetic properties of Ni–Zn ferrites - ScienceDirect, Journal of Magnetism and Magnetic Materials, 256 (2003) 174-182.

[3] T.J. Shinde, A.B. Gadkari, P.N. Vasambekar, Magnetic properties and cation distribution study of nanocrystalline Ni–Zn ferrites, Journal of Magnetism and Magnetic Materials, 333 (2013) 152-155.

[4] G.V. Bazuev, O.I. Gyrdasova, S.I. Novikov, A.Y. Kuznetsov, Synthesis, structure, and magnetic properties of rare-earth-doped Ni0.75Zn0.25Fe2O4 nickel zinc ferrite, Inorganic Materials, 52 (2016) 932-938.

[5] J.-L. Mattei, D. Souriou, A. Chevalier, Magnetic and dielectric properties in the UHF frequency band of half-dense Ni-Zn-Co ferrites ceramics with Fe-excess and Fe-deficiency, Journal of Magnetism and Magnetic Materials, 447 (2018) 9-14.

[6] N. Sanchayita, R. Anirban, D. Dipankar, D. Sukhen, M. Sampad, Structural and magnetic properties of erbium (Er 3+) doped nickel zinc ferrite prepared by sol-gel auto-combustion method, Journal of Magnetism and Magnetic Materials, 466 (2018) S0304885317311472-.

[7] N. Boda, G. Boda, K.C.B. Naidu, M. Srinivas, K.M. Batoo, D. Ravinder, A.P. Reddy, Effect of rare earth elements on low temperature magnetic properties of Ni and Co-ferrite nanoparticles, Journal of Magnetism and Magnetic Materials, 473 (2019) 228-235.

[8] P.H. Nam, N.X. Phuc, D.K. Tung, V.Q. Nguyen, N.H. Nam, D.H. Manh, P.T. Phong, Effect of superparamagnetic interaction on the magnetic heating efficiency of Co0.3Zn0.7Fe2O4 and Co0.5Zn0.5Fe2O4 nanoparticles, Physica B: Condensed Matter, 591 (2020).

[9] N. Kaur, B. Chudasama, Tunable Curie temperature of Mn0.6Zn0.4Fe2O4 nanoparticles, Journal of Magnetism and Magnetic Materials, 465 (2018) 164-168.

[10] S.I. Ahmad, S.A. Ansari, D. Ravi Kumar, Structural, morphological, magnetic properties and cation distribution of Ce and Sm co-substituted nano crystalline cobalt ferrite, Materials Chemistry and Physics, 208 (2018) 248-257.

[11] S.M. Ognjanovic, I. Tokic, Z. Cvejic, S. Rakic, V.V. Srdic, Structural and dielectric properties of yttrium substituted nickel ferrites, Materials Research Bulletin, 49 (2014) 259-264.

[12] N.I. Abu-Elsaad, A.S. Nawara, S.A. Mazen, Synthesis, structural characterization, and magnetic properties of Ni–Zn nanoferrites substituted with different metal ions (Mn2+, Co2+, and Cu2+), Journal of Physics and Chemistry of Solids, 146 (2020).

[13] M.A. Almessiere, A.D. Korkmaz, Y. Slimani, M. Nawaz, S. Ali, A. Baykal, Magneto-optical properties of rare earth metals substituted Co-Zn spinel nanoferrites, Ceramics International, 45 (2019) 3449-3458.

[14] R.K. Singh, J. Shah, R.K. Kotnala, Magnetic and dielectric properties of rare earth substituted Ni0.5Zn0.5Fe1.95R0.05O4 (R = Pr, Sm and La) ferrite nanoparticles, Materials Science and Engineering: B, 210 (2016) 64-69.

[15] S.E. Jacobo, M. Arana, P.G. Bercoff, Gadolinium substitution effect on the thermomagnetic properties of Ni ferrite ferrofluids, Journal of Magnetism and Magnetic Materials, 415 (2016) 30-34.

[16] K.K. Bamzai, G. Kour, B. Kaur, S.D. Kulkarni, Effect of cation distribution on structural and magnetic properties of Dy substituted magnesium ferrite, Journal of Magnetism and Magnetic Materials, 327 (2013) 159-166.

[17] R.A. Pawar, S.M. Patange, A.R. Shitre, S.K. Gore, S.S. Jadhav, S.E. Shirsath, Crystal chemistry and single-phase synthesis of Gd3+substituted Co–Zn ferrite nanoparticles for enhanced magnetic properties, RSC Advances, 8 (2018) 25258-25267.

[18] N. Hamdaoui, Y. Azizian-Kalandaragh, M. Khlifi, L. Beji, Structural, magnetic and dielectric properties of Ni0.6Mg0.4Fe2O4 ferromagnetic ferrite prepared by sol gel method, Ceramics International, 45 (2019) 16458-16465.

[19] R. Raeisi Shahraki, M. Ebrahimi, S.A. Seyyed Ebrahimi, S.M. Masoudpanah, Structural characterization and magnetic properties of superparamagnetic zinc ferrite nanoparticles synthesized by the coprecipitation method, Journal of Magnetism and Magnetic Materials, 324 (2012) 3762-3765.

[20] R. Kesavamoorthi, C.R. Raja, Substitution Effects on Rare-Earth Ions-Doped Nickel-Zinc Ferrite Nanoparticles, Journal of Superconductivity and Novel Magnetism, 30 (2016) 1207-1212.

[21] I. Soibam, S. Phanjoubam, H.B. Sharma, H.N.K. Sarma, C. Prakash, Magnetic studies of Li–Zn ferrites prepared by citrate precursor method, Physica B: Condensed Matter, 404 (2009) 3839-3841.

[22] D. Makovec, A. Košak, A. Žnidaršič, M. Drofenik, The synthesis of spinel–ferrite nanoparticles using precipitation in microemulsions for ferrofluid applications, Journal of Magnetism and Magnetic Materials, 289 (2005) 32-35.

[23] P. Pahuja, R.K. Kotnala, R.P. Tandon, Effect of rare earth substitution on properties of barium strontium titanate ceramic and its multiferroic composite with nickel cobalt ferrite, Journal of Alloys and Compounds, 617 (2014) 140-148.

[24] L.B. de Mello, L.C. Varanda, F.A. Sigoli, I.O. Mazali, Coprecipitation synthesis of (Zn-Mn)-co-doped magnetite nanoparticles and their application in magnetic hyperthermia, Journal of Alloys and Compounds, 779 (2019) 698-705.

[25] P. Thakur, S. Taneja, D. Sindhu, U. Lüders, A. Sharma, B. Ravelo, A. Thakur, Manganese Zinc Ferrites: a Short Review on Synthesis and Characterization, Journal of Superconductivity and Novel Magnetism, 33 (2020) 1569-1584.

[26] S. Amiri, H. Shokrollahi, Magnetic and structural properties of RE doped Co-ferrite (REåNd, Eu, and Gd) nano-particles synthesized by coprecipitation, Journal of Magnetism and Magnetic Materials, 345 (2013) 18-23.

[27] T.J. Shinde, A.B. Gadkari, P.N. Vasambekar, Effect of Nd3+ substitution on structural and electrical properties of nanocrystalline zinc ferrite, Journal of Magnetism and Magnetic Materials, 322 (2010) 2777-2781.

[28] X. Wu, Z. Ding, N. Song, L. Li, W. Wang, Effect of the rare-earth substitution on the structural, magnetic and adsorption properties in cobalt ferrite nanoparticles, Ceramics International, 42 (2016) 4246-4255.

[29] X. Zhou, Y. Zhou, L. Zhou, J. Wei, J. Wu, D. Yao, Effect of Gd and La doping on the structure, optical and magnetic properties of NiZnCo ferrites, Ceramics International, 45 (2019) 6236-6242.

[30] S. Ikram, F. Ashraf, M. Alzaid, K. Mahmood, N. Amin, S.A. Haider, Role of Nature of Rare Earth Ion Dopants on Structural, Spectral, and Magnetic Properties in Spinel Ferrites, Journal of Superconductivity and Novel Magnetism, (2020).

[31] Z. Liu, Z. Peng, C. Lv, X. Fu, Doping effect of Sm 3+ on magnetic and dielectric properties of Ni-Zn ferrites, Ceramics International, 43 (2017) 1449-1454.

[32] C.C. Naik, A.V. Salker, Structural, magnetic and dielectric properties of Dy3+ and Sm3+ substituted Co–Cu ferrite, Materials Research Express, 6 (2019).

[33] Z. Bitar, W. Abdeen, R. Awad, Effect of Er~(3+) and Pr~(3+) on the structural, magnetic and dielectric properties of Zn-Co ferrite synthesised via coprecipitation method, Materials Research Innovations, 24 (2020) 104-112.

[34] M. Sertkol, Y. Köseoğlu, A. Baykal, H. Kavas, A. Bozkurt, M.S. Toprak, Microwave synthesis and characterization of Zn-doped nickel ferrite nanoparticles, Journal of Alloys and Compounds, 486 (2009) 325-329.

[35] F. Moravvej-Farshi, M. Amishi, K.A. Nekouee, Influence of different milling time on synthesized Ni–Zn ferrite properties by mechanical alloying method, Journal of Materials Science: Materials in Electronics, 31 (2020) 13610-13619.

[36] M. Kumari, M.C. Bhatnagar, Study of the Effect of Pr Doping on Structural, Morphological and Magnetic Properties of Nickel Ferrite, Journal of Superconductivity and Novel Magnetism, 32 (2018) 1027-1033.

[37] G. Umapathy, G. Senguttuvan, L.J. Berchmans, V. Sivakumar, P. Jegatheesan, Influence of cerium substitution on structural, magnetic and dielectric properties of nanocrystalline Ni–Zn ferrites synthesized by combustion method, Journal of Materials Science: Materials in Electronics, 28 (2017) 17505-17515.

[38] V. Jagadeesha Angadi, B. Rudraswamy, K. Sadhana, S.R. Murthy, K. Praveena, Effect of Sm3+ –Gd3+ on structural, electrical and magnetic properties of Mn–Zn ferrites synthesized via combustion route, Journal of Alloys and Compounds, 656 (2016) 5-12.

[39] X. Zhao, A. Sun, W. Zhang, Y. Han, X. Pan, Effects of Mg Substitution on the Structural and Magnetic Properties of Ni0.2MgxCo0.8−xFe2O4 Nanoparticle Ferrites, Journal of Superconductivity and Novel Magnetism, 32 (2019) 2589-2598.

[40] M.A. Almessiere, Y. Slimani, A. Demir Korkmaz, S. Guner, A. Baykal, S.E. Shirsath, I. Ercan, P. Kogerler, Sonochemical synthesis of Dy3+ substituted Mn0.5Zn0.5Fe2-xO4 nanoparticles: Structural, magnetic and optical characterizations, Ultrasonics sonochemistry, 61 (2019) 104836-104836.

[41] A. Kumar, P.S. Rana, M.S. Yadav, R.P. Pant, Effect of Gd3+ ion distribution on structural and magnetic properties in nano-sized Mn–Zn ferrite particles, Ceramics International, 41 (2015) 1297-1302.

[42] V. Verma, R.K. Kotnala , V. Pandey, P.C. Kothari , L. Radhapiyari, B.S. Matheru, The effect on dielectric losses in lithium ferrite by cerium substitution, Journal of Alloys and Compounds 466 (2008) 404-407.

[43] S. Joshi, M. Kumar, H. Pandey, M. Singh, P. Pal, Structural, magnetic and dielectric properties of Gd3+ substituted NiFe2O4 nanoparticles, Journal of Alloys and Compounds, 768 (2018) 287-297.

[44] S. Aslam, M. Shahzad Shifa, Z. Abbas Gilani, H.M. Noor ul Huda Khan Asghar, M. Nauman Usmani, J. Ur Rehman, M. Azhar Khan, A. Perveen, M. Khalid, Structural, optical and magnetic elucidation of co-doping of Nd3+ and Pr3+ on lithium nanoferrite and its technological application, Results in Physics, 12 (2019) 1334-1339.

[45] J. Hu, Y. Ma, X. Kan, C. Liu, X. Zhang, R. Rao, M. Wang, G. Zheng, Investigations of Co substitution on the structural and magnetic properties of Ni-Zn spinel ferrite, Journal of Magnetism and Magnetic Materials, 513 (2020).

[46] C.C. Chauhan, A.R. Kagdi, R.B. Jotania, A. Upadhyay, C.S. Sandhu, S.E. Shirsath, S.S. Meena, Structural, magnetic and dielectric properties of Co-Zr substituted M-type calcium hexagonal ferrite nanoparticles in the presence of α-Fe2O3 phase, Ceramics International, 44 (2018) 17812-17823.

[47] T.A. Nhlapo, T. Moyo, The effect of particle size on structural and magnetic properties of Sm3+ ion substituted Zn-Mn nanoferrites synthesized by glycol-thermal method, Journal of Magnetism and Magnetic Materials, 513 (2020).

[48] S. Urcia-Romero, O. Perales-Pérez, G. Gutiérrez, Effect of Dy-doping on the structural and magnetic properties of Co–Zn ferrite nanocrystals for magnetocaloric applications, Journal of Applied Physics, 107 (2010).

Figures

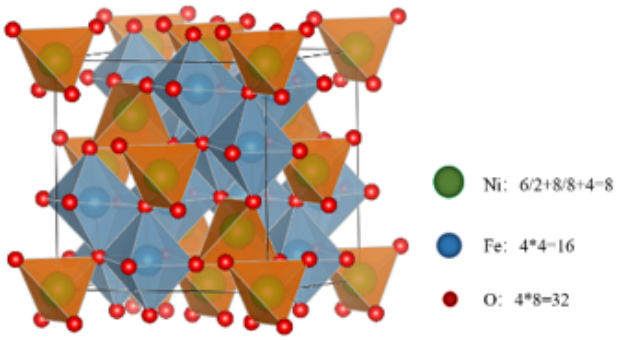

Figure 1

Crystallographic texture of Ni-Zn spinel ferrite (Prepared by software VESTA)

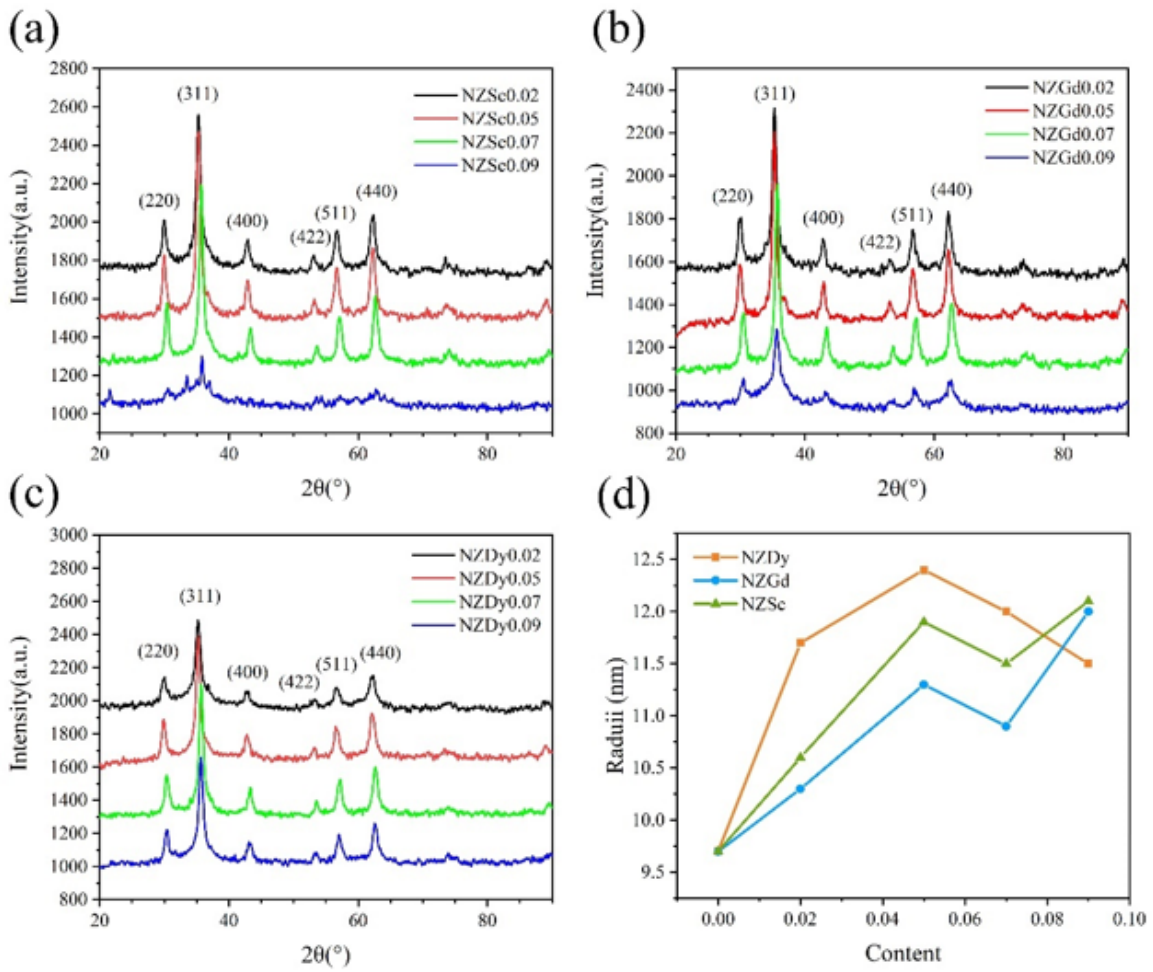

Figure 2

XRD patterns and radius for Ni0.5Zn0.5RexFe2-xO4 (RE = Sc, Gd, Dy, X = 0.02, 0.05, 0.07 and 0.09)

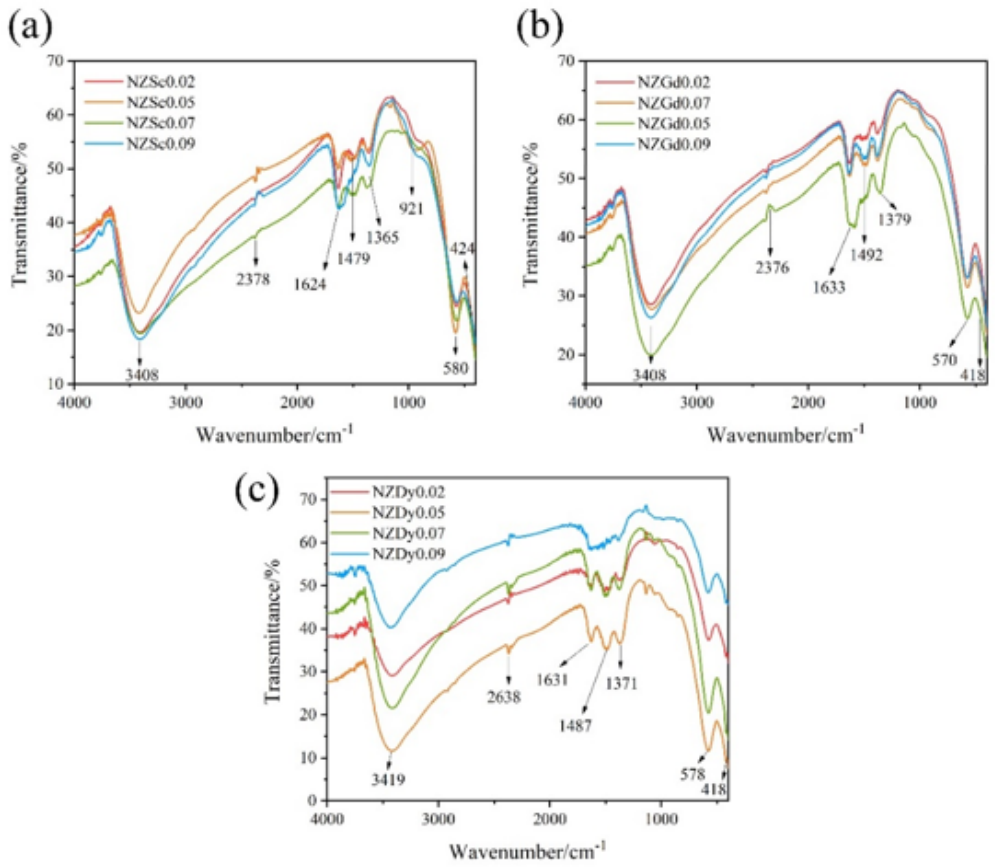

Figure 3

FTIR spectra of the Ni0.5Zn0.5RexFe2-xO4 samples (RE = Dy, Gd, Sc□x = 0.02, 0.05, 0.07, 0.09)

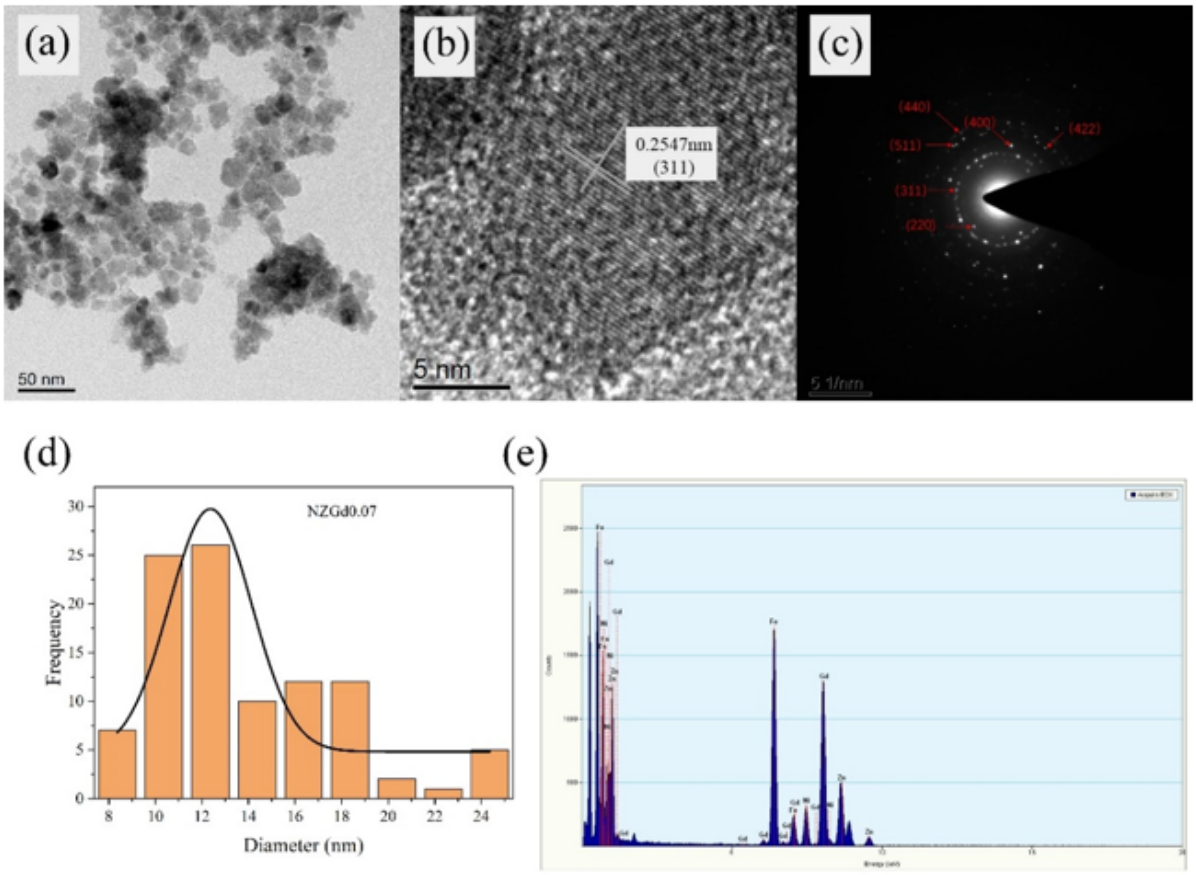

Figure 4

(a) Transmission electron microscopy of NZGd0.07 (b) HRTEM images of representative NZGd0.07 nanoparticles (c) SAED pattern of the corresponding NZGd0.07 (d) Size histogram of NZGd0.07 (e) Energy dispersive x-ray Spectra of NZGd0.07

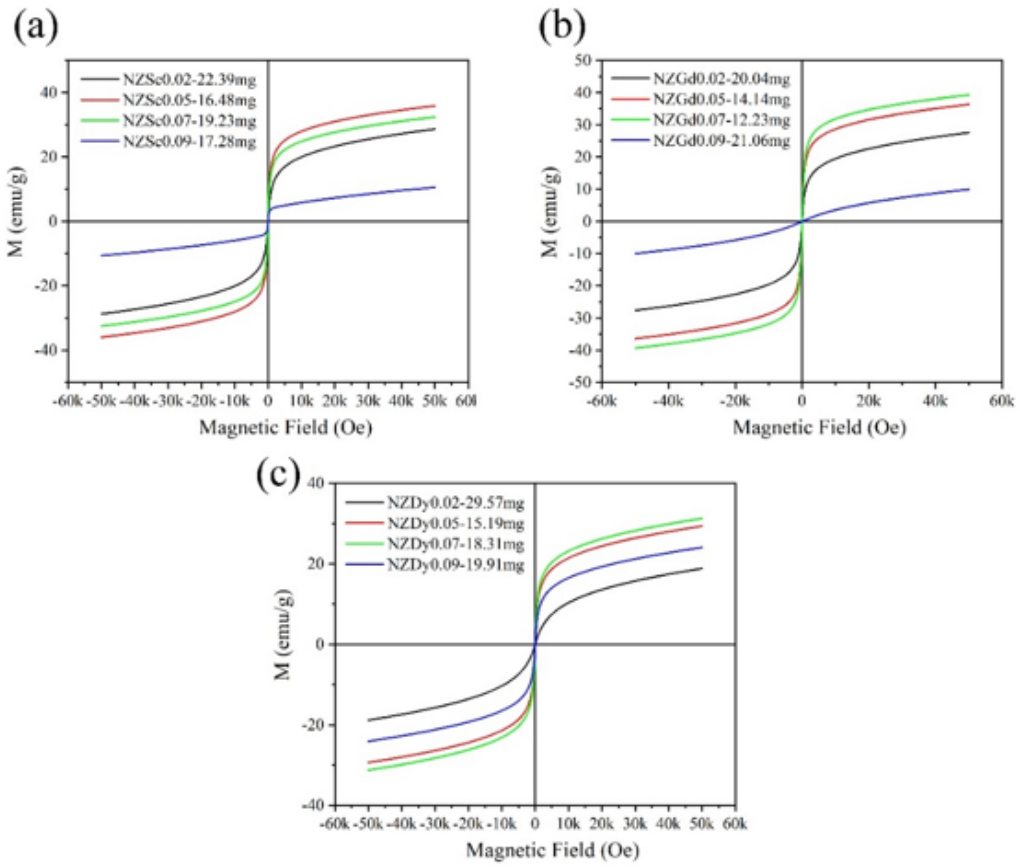

Figure 5

Magnetization curve of Ni0.5Zn0.5RexFe2-xO4 samples (RE = Dy, Gd, Sc, x = 0.02, 0.05, 0.07, 0.09) at room temperature (293 K)

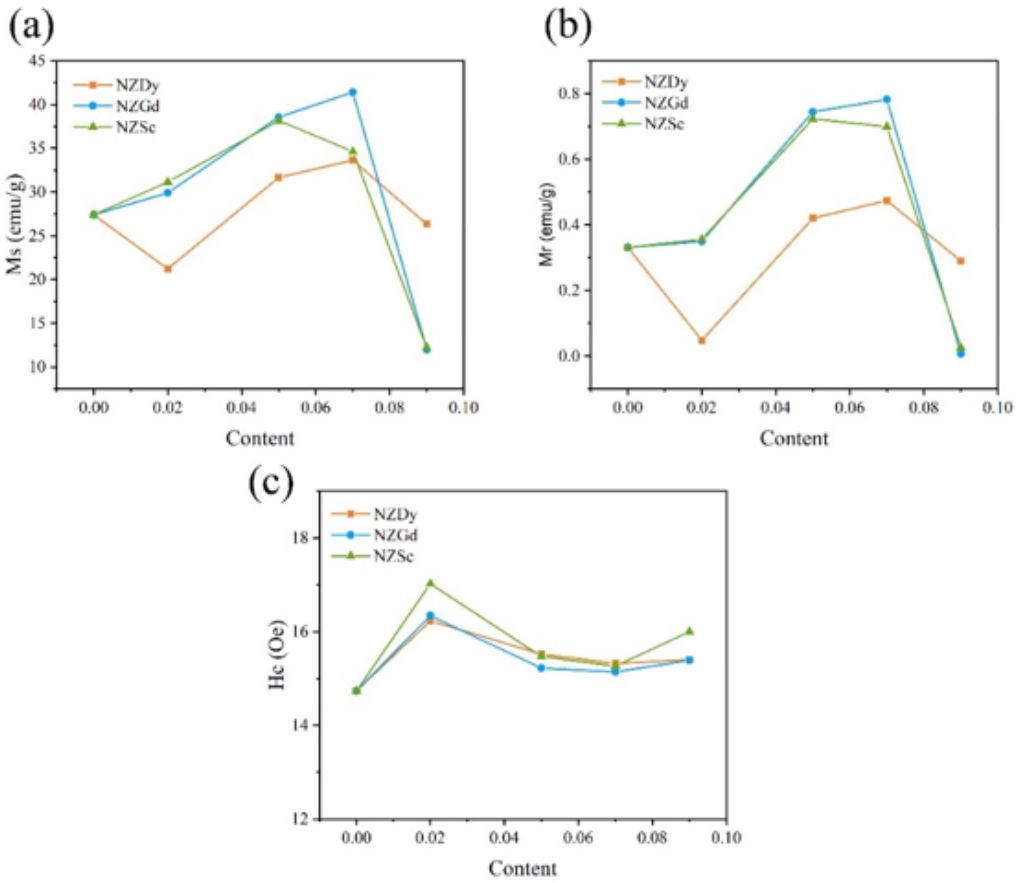

Figure 6

Variations of MS and HC values for, Ni0.5Zn0.5RexFe2-xO4 samples (RE = Dy, Gd, Sc, x = 0.02, 0.05, 0.07, 0.09) with respect to the content at room temperature (293 K)

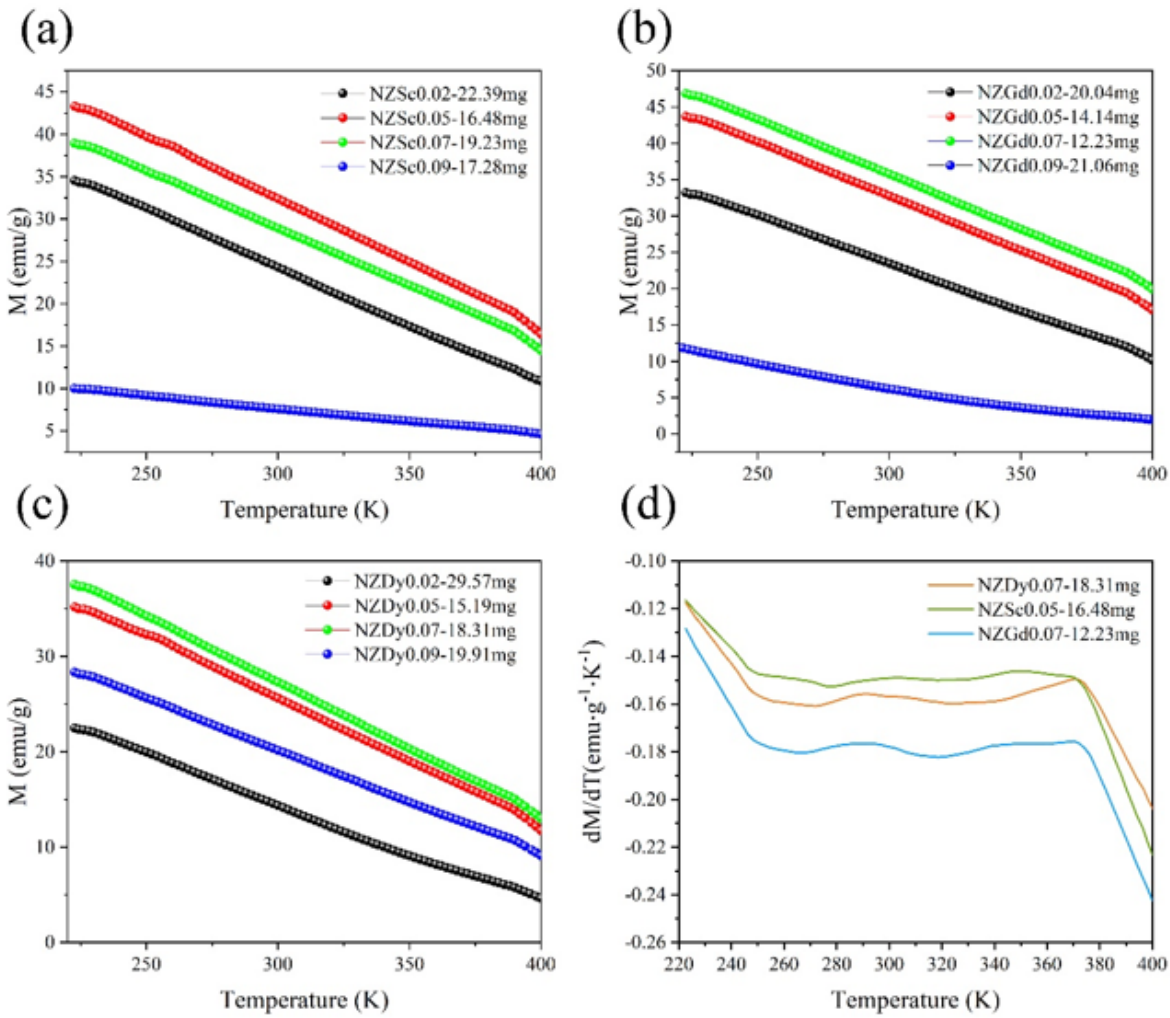

Figure 7

Magnetization measurements as a function of temperature for Ni0.5Zn0.5RexFe2-xO4 samples (RE = Dy, Gd, Sc, x = 0.02, 0.05, 0.07, 0.09) under 2T

Supplementary Files

This is a list of supplementary files associated with this preprint. Click to download.

- renamed20670.pptx